

Effect of Spin-Orbit Coupling in non-centrosymmetric half-Heusler alloys

Kunal Dutta, Subhadeep Bandyopadhyay,* and Indra Dasgupta†
School of Physical Sciences, Indian Association for the Cultivation of Science,
2A and 2B Raja S.C. Mullick Road, Jadavpur, Kolkata 700 032, India
(Dated: November 2, 2023)

Spin-orbit coupled electronic structure of two representative non-polar half-Heusler alloys, namely 18 electron compound CoZrBi and 8 electron compound SiLiIn have been studied in detail. An excursion through the Brillouin zone of these alloys from one high symmetry point to the other revealed rich local symmetry of the associated wave vectors resulting in non-trivial spin splitting of the bands and consequent diverse spin textures in the presence of spin-orbit coupling. Our first principles calculations supplemented with low energy $\mathbf{k}\cdot\mathbf{p}$ model Hamiltonian revealed the presence of linear Dresselhaus effect at the X point having D_{2d} symmetry and Rashba effect with both linear and non-linear terms at the L point with C_{3v} point group symmetry. Interestingly we have also identified non-trivial Zeeman spin splitting at the non-time reversal invariant W point and a pair of non-degenerate bands along the path Γ to L displaying vanishing spin polarization due to the non-pseudo polar point group symmetry of the wave vectors. Further a comparative study of CoZrBi and SiLiIn suggest, in addition to the local symmetry of the wave vectors, important role of the participating orbitals in deciding the magnitude of the spin splitting of the bands. Our calculations suggest half-Heusler compounds with heavy elements displaying diverse spin textures may be ideal candidate for spin valleytronics where spin textures can be controlled by accessing different valleys around the high symmetry k-points.

I. INTRODUCTION

In non-centrosymmetric systems, the non-vanishing gradient of the electrostatic potential results in a momentum dependent magnetic field $\mathbf{\Omega}(\mathbf{k})$ in the rest frame of the electron. The coupling of this field with the spin $\vec{\sigma}$ of the electron lifts the spin-degeneracy of the bands in an otherwise non-magnetic system. The resulting spin-orbit coupled Hamiltonian is given by, $H_{SOC} = \mathbf{\Omega}(\mathbf{k}) \cdot \vec{\sigma}$. Depending on the symmetry, $\mathbf{\Omega}(\mathbf{k})$ may have both linear and higher order k-dependent terms. The momentum dependent field $\mathbf{\Omega}(\mathbf{k})$ that locks the electron's spin direction to its momentum not only remove the spin degeneracy of the bands but also leads to complex spin textures in the reciprocal space. Spin texture(ST) is the expectation value of the spin operator $\langle \vec{S}_n(\mathbf{k}) \rangle$ in a given Bloch wave function $u_n(\mathbf{k})$ around a specific k-point, where n is the band index. Spin textures depending on the symmetry may display Rashba¹, Dresselhaus², persistent³, radial⁴ or more complex spin configurations in the momentum space. In addition to the well studied Dresselhaus and Rashba effect that leads to splitting of non-degenerate bands with characteristic ST in non-centrosymmetric systems, there are also other possibilities where spin degeneracy can be lifted in non-magnetic, non-centrosymmetric systems due to the presence of $\mathbf{\Omega}(\mathbf{k})$.

It is well known that in materials either with intrinsic magnetic ordering or in the presence of a magnetic field, time reversal(TR) symmetry is broken, leading to splitting of energy bands with opposite spins, referred to as, Zeeman spin splitting⁵. In nonmagnetic, non-centrosymmetric compounds, a combination of non-time reversal invariant k-point and lack of inversion symmetry in the presence of spin-orbit coupling(SOC) also leads to

spin splitting of bands in the momentum space similar to the Zeeman effect⁶. Further it has been recently shown the possibility of spin splitting of bands in a non-magnetic, non-centrosymmetric crystals in the presence of SOC, where the split bands does not show any net spin polarization around certain high symmetry points of the Brillouin zone (BZ)⁷. Such systems with band splitting having vanishing spin polarisation offers the possibility of tuning spin polarization either with the application of an electric field or strain that may be important for spintronics application.

Earlier research on Dresselhaus effect have primarily focused on materials in which the bulk exhibits inversion asymmetry. It was originally proposed for non-polar zinc-blende semiconductors, where the splitting of the band is proportional to k^3 ². On the other hand the Rashba effect was proposed for non-centrosymmetric polar wurtzite structure displaying linear splitting of bands⁸. The search for Rashba effect was initially confined to 2D surfaces, interfaces. In view of the above, Rashba splitting was observed on surfaces of heavy metals, such as Au (111)⁹ and Bi (111)¹⁰, at the surface of oxides such as SrTiO₃ (001)¹¹ and KTaO₃ (001)¹², on the two dimensional materials¹³⁻¹⁵, and on hetero-structure interfaces such as InGaAs/InAlAs¹⁶ and LaAlO₃/SrTiO₃¹⁷. However recent studies on bulk polar materials show large Rashba spin splitting for e.g. in BiTeX (X = Cl, Br, I)¹⁸⁻²⁰ and GeTe^{21,22}. Recently it has been reported that both Dresselhaus and Rashba spin splitting is also observed in bulk ferroelectric oxide perovskites such as BiAlO₃²³, HfO₂²⁴ and nitride perovskite LaWN₃²⁵. Further recent studies suggest that the Rashba effect occurs not only in bulk for polar and ferroelectric crystal structures, but may also occur in non-polar crystals with polar point group in the BZ²⁶.

The Zeeman effect on the other hand was observed in the two-dimensional WSe₂ and MoS₂^{27,28}, and a large Zeeman splitting was also observed in bulk OsC, WN₂, SnTe²⁹ and in the non-polar GaAs³⁰. Band splitting with vanishing spin polarisation was suggested to be realised in bulk nonsymmorphic GaAs and symmorphic 2D-SnTe⁷.

While crystallographic point group symmetry (CPGS) was originally attributed to be responsible for the nature of spin textures (Rashba or Dresselhaus type), very recently it was observed that the point group symmetry of the wave vector (little group)²⁶ and the symmetry of the orbitals involved³¹ play a crucial role in determining the spin textures. As a consequence, in the same compound diverse spin textures can be realised around different high symmetry k-points of the BZ depending on its little group. Similarly different compounds at a particular k-point despite having same little group, depending on the orbital character of the bands may display diverse spin textures³¹.

In this paper, we have considered two representative semiconducting half-Heusler compounds with heavy elements having 18 and 8 valence electrons respectively. The unique non-polar crystal structure of the half-Heusler compounds where the ternary half-Heusler is a combination of two binaries, one with centrosymmetric and the other with non-centrosymmetric structure will be shown to host variety of spin textures depending on the symmetry of the k-points in the BZ. Our calculations clearly identify the importance of the little group of the chosen k-point in determining the nature of the spin textures. A comparative study of the two half-Heusler compounds show that the orbital character of the bands are important in deciding the strength of the SOC induced band splitting.

The rest of the paper is organized as follows. Sec. II is devoted to the description of the structural properties of non-polar half-Heusler compounds and details of the computational methods. In Sec. III we have discussed the results of our first principles electronic structure calculations. Sec. IV is devoted to the description of the nature of band splitting and consequent spin textures at various high symmetry k-points of the BZ. The results of our first principle calculations have been analysed here in the framework of a low energy $\mathbf{k}\cdot\mathbf{p}$ model. Finally, conclusions are presented in Sec. V.

TABLE I. The lattice constant and atomic positions for bulk half-Heusler compounds.

Space group	Bulk half-Heusler	$a(\text{\AA})$	Site	x	y	z
$F\bar{4}3m$ (216)	18 electron CoZrBi	6.23 ³²	Zr(4a)	0.00	0.00	0.00
			Co(4c)	0.25	0.25	0.25
			Bi(4b)	0.50	0.50	0.50
	8 electron SiLiIn	6.31 ³³	Li(4a)	0.00	0.00	0.00
			Si(4c)	0.25	0.25	0.25
			In(4b)	0.50	0.50	0.50

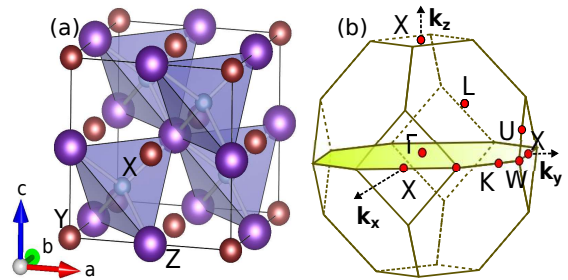


FIG. 1. (a) Crystal structure and (b) BZ of bulk half-Heusler compounds. The half-Heusler compound have XYZ composition, where X(Co, Si) have higher valence compared to Y(Zr, Li) and, Y and Z(Bi, In) form a rock salt structure.

II. STRUCTURAL AND COMPUTATIONAL DETAILS

The half-Heusler compound XYZ crystallize in the face-centered cubic structure with one formula unit per primitive unit cell, as shown in Fig. 1(a). In normal half-Heusler alloys, X and Y are transition metals with X being higher valence element in comparison to Y, and Z is a sp valent element. The space group is $F\bar{4}3m$ (No. 216). In the conventional stable structure Y and Z atoms are located at $4a(0, 0, 0)$ and $4b(\frac{1}{2}, \frac{1}{2}, \frac{1}{2})$ positions forming the rock salt structure arrangement and the X atom is located in the tetrahedrally coordinated pocket, at one of the cube center positions $4c(\frac{1}{4}, \frac{1}{4}, \frac{1}{4})$ leaving the other $4c(\frac{3}{4}, \frac{3}{4}, \frac{3}{4})$ empty, resulting in the absence of inversion symmetry. We shall consider a representative semiconducting 18 valence electron half-Heusler compound CoZrBi³². In addition, we have also considered a representative semiconducting sp valent compound SiLiIn³³ featuring half-Heusler structure with 8 valence electrons.

The calculations presented in this paper have been carried out using Vienna *ab initio* simulation package (VASP)^{34,35} within density-functional theory (DFT) using the supplied projector augmented-wave pseudo potentials^{36,37} and Perdew-Burke-Ernzerhof generalized gradient approximation (GGA)³⁸. Here the energy cutoff has been set to 600 eV for the calculations and a $10 \times 10 \times 10$ k-point mesh is used for the self-consistent calculations using the Monkhorst grid for k-point sampling. All the calculations are done with experimental lattice constant. The details of the structure, including structural parameters are summarised in Table I.

Fig. 1(b) represents the BZ of the face-centered cubic half-Heusler compound. The various high symmetry points of the BZ are Γ at the center of the BZ, L at the center of each hexagonal face, X at the center of each square face, W at each corner formed from one square and two hexagons, K at middle of an edge joining two hexagonal faces. Further X point has 6 fold-degeneracy, L point has 8 fold degeneracy, W and K points have 12 fold degeneracy. In the BZ, except W and K points all are

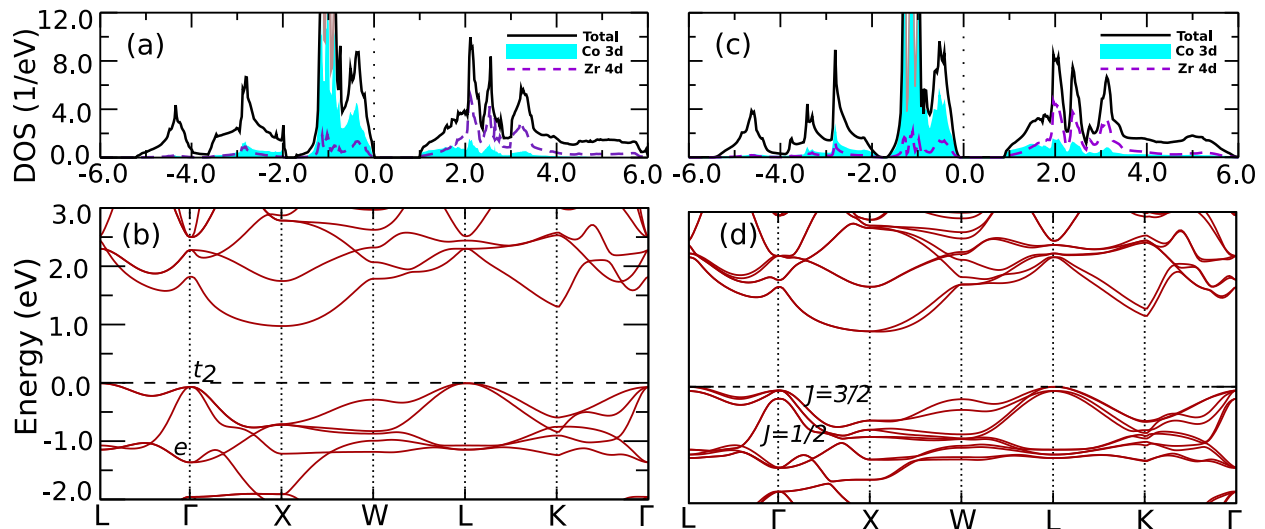


FIG. 2. The density of states and electronic band structure of the 18 electron half-Heusler compound CoZrBi, in the absence and presence of SOC. In (a) and (c) the total and projected DOS for the Co-3d and Zr-4d are shown without and with SOC respectively. (b) and (d) Displays the band structure along various high symmetry points of the BZ in absence and presence of SOC respectively. The band structures of CoZrBi are plotted along the high-symmetry points $L(\frac{\pi}{a}, \frac{\pi}{a}, \frac{\pi}{a})-\Gamma(0, 0, 0)-X(0, \frac{2\pi}{a}, 0)-W(\frac{\pi}{a}, \frac{2\pi}{a}, 0)-L(\frac{\pi}{a}, \frac{\pi}{a}, \frac{\pi}{a})-K(\frac{3\pi}{2a}, \frac{3\pi}{2a}, 0)-\Gamma(0, 0, 0)$ of the BZ. The Fermi level is aligned to the valence-band maximum with zero value in the energy axis.

time reversal(TR) invariant. A time reversal invariant k-point³⁹ satisfies the condition $-\mathbf{k} + \mathbf{G} = \mathbf{k}$, where \mathbf{G} is the reciprocal lattice vector.

III. ELECTRONIC STRUCTURE CALCULATIONS

To begin with we have analysed the density of states without SOC for the 18 electron compound CoZrBi obtained from DFT calculations. The non-spin-polarized total as well as projected density of states of Co-3d and Zr-4d have been shown in Fig. 2(a). The characteristic feature of the total DOS is a pair of bonding and antibonding states resulting from the covalent hybridization of the higher valence Co-d and lower valence Zr-d states separated by a 0.98 eV gap at the Fermi level⁴⁰. Below the bonding states are the Bi-p states separated by a p-d gap. Below the Bi-p state lies the Bi-s state. The semiconducting nature of the compound can be understood from the electron filling of the system. As the total number of valence electrons of the system is 18, these are accommodated in the available Bi-s, Bi-p and the bonding partner of the Co-d - Zr-d hybridised states. The Co-d and Zr-d projected DOS reveal that the bonding states have primary contribution from the 3d states of Co, while the antibonding states are primarily composed of Zr-d states.

In Fig. 2(b) we have shown the band structure of CoZrBi around the Fermi level. An indirect band gap of 0.98 eV is observed between the L point of the valence band and the X point of the conduction band,

in agreement with a previous report⁴¹. Further due to the tetrahedral network, at the Γ point, the top of the valence band consisting of Co-Zr d-states split into 3-fold degenerate t_2 and 2-fold degenerate e states, with the latter lying lower in energy.

Fig. 2[(c) and (d)] display DOS and band structure of CoZrBi including SOC. The gross feature of the DOS is very similar to that obtained without SOC, except for the presence of additional splittings and the value of the d-d gap is now 0.96 eV. However the non trivial effect of the absence of inversion symmetry upon inclusion of SOC is revealed in the band structure shown in Fig. 2(d). The effect of the SOC depends on the symmetry of the paths in the reciprocal space. The spin degeneracy of the bands along various high symmetry direction of the BZ are lifted. Of particular interest is the top of the valence band at the Γ point, where SOC further splits the t_2 states into four fold degenerate $J = \frac{3}{2}$ and a two fold degenerate $J = \frac{1}{2}$ states with the latter lying lower in energy in the tetrahedral environment. Unlike the t_2 states, the e -states retain their degeneracy at the Γ point.

The total as well as the projected DOS and the band structure around the Fermi level without SOC for the 8 electron half-Heusler SiLiIn is shown in Fig. 3(a) and Fig. 3(b) respectively. Similar to the 18 electron compound the characteristic feature of the DOS is a pair of bonding and antibonding states derived from In s+p and Si s+p separated by a semiconducting gap of magnitude 0.12 eV. Below the bonding state lies the Si-s state. As the total number of valence electrons of the system is 8, these are accommodated in the Si-s state and bonding partner of the p-states below the Fermi level. The plot of the

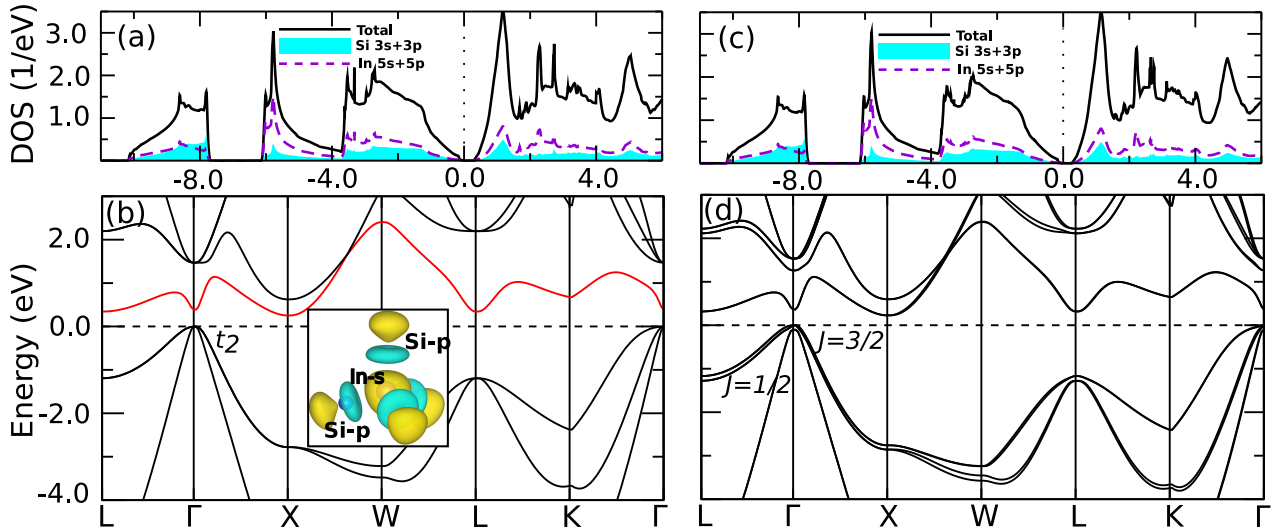


FIG. 3. The density of states and electronic band structure of the 8 electron half-Heusler compound SiLiIn, in the absence and presence of SOC. In (a) and (c) the total and projected DOS for the Si-3s+3p and In-5s+5p are shown without and with SOC respectively. (b) and (d) Displays the band structure along various high symmetry points of the BZ in absence and presence of SOC respectively. The band structures of SiLiIn are plotted along the high-symmetry points $L(\frac{\pi}{a}, \frac{\pi}{a}, \frac{\pi}{a})$ - $\Gamma(0, 0, 0)$ - $X(0, \frac{2\pi}{a}, 0)$ - $W(\frac{\pi}{a}, \frac{2\pi}{a}, 0)$ - $L(\frac{\pi}{a}, \frac{\pi}{a}, \frac{\pi}{a})$ - $K(\frac{3\pi}{2a}, \frac{3\pi}{2a}, 0)$ - $\Gamma(0, 0, 0)$ of the BZ. Fermi level is aligned to the valence-band maximum with zero value in the energy axis. The inset in (b) represents the Wannier function of the lowest conduction band.

band structure reveal an indirect band gap of 0.12 eV between the Γ point of the valence band and the X point of the conduction band. The top of the valence band at the Γ point is the 3-fold degenerate p-band. The lowest conduction band is predominantly sp^3 hybridized In-s - Si-p band (see Fig. 3(b) inset).

Finally the DOS and band structure of SiLiIn including SOC is shown in Fig. 3[(c),(d)]. The gross feature of the DOS is very similar to that without SOC shown in Fig. 3(a) except for additional splittings. As expected, around the Γ point of the valence band, the three fold degenerate p-bands splits into $J = \frac{3}{2}$ and $J = \frac{1}{2}$ states, where the splitting is much smaller in comparison to the 18 electron compound.

IV. NATURE OF BAND SPLITTING AND SPIN TEXTURES

Next we have analysed the nature of the SOC induced splitting of the bands near various high symmetry points of the BZ, in order to elucidate the importance of local symmetry. In the following, we have discussed in detail the spin orbital locked split bands and the novel spin textures displayed by them in the k -space at and around the TR invariant non-polar(X), polar(L) and non-time reversal invariant W points, which based on local symmetry are expected to display Dresselhaus effect, Rashba effect and Zeeman effect respectively.

A. Dresselhaus and Rashba effect

1. X point($0, 0, \frac{2\pi}{a}$)

To begin with we have analysed the conduction band minimum(CBM) of CoZrBi around the neighborhood of the high symmetry non-polar X point along the path $W(\frac{\pi}{a}, 0, \frac{2\pi}{a})$ - $X(0, 0, \frac{2\pi}{a})$ - $W(0, \frac{\pi}{a}, \frac{2\pi}{a})$ in the $k_z = \frac{2\pi}{a}$ plane. The DFT band structure for CoZrBi in a narrow k -range along the above mentioned path, without and including SOC are displayed in Fig. 4(a) and 4(b) respectively. The band structure including SOC shows that the band minimum is shifted from the X point in both directions, reminiscent of Rashba-Dresselhaus effect. In order to identify the nature of the spin splitting, the ST of the inner and outer branches of the CBM around the X point has been shown in Fig. 4(c) and 4(d) respectively. As shown in Fig. 4[(c), (d)], the angle between the \mathbf{k} and the expectation values of spin $\langle S_x \rangle$ and $\langle S_y \rangle$ varies with the direction and the $\langle S_z \rangle$ component is absent. Along the k_x and k_y axis, the spin is parallel to \mathbf{k} , while it is perpendicular to \mathbf{k} along the diagonals. As expected the direction of the spin textures are opposite for the inner and outer branches as shown in 4(c) and 4(d) respectively. These are characteristic signatures of linear Dresselhaus effect. In order to understand our DFT results next we have derived a low energy $\mathbf{k}\cdot\mathbf{p}$ model Hamiltonian.

The point-group, symmetry around the X($0, 0, \frac{2\pi}{a}$) point is D_{2d} having twofold $C_2(z)$ rotation around the z axis(principle axis), twofold rotation perpendicular

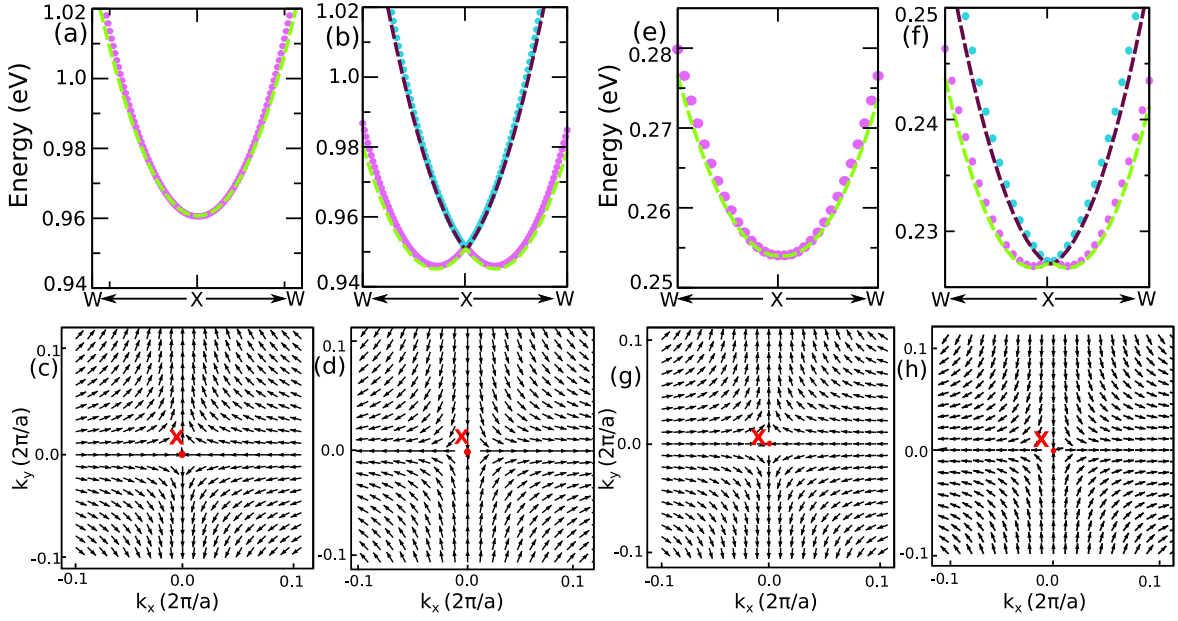


FIG. 4. The band structure and ST of CoZrBi and SiLiIn plotted in the $k_z = \frac{2\pi}{a}$ plane in a very narrow k -range around the X point in the presence and absence of SOC. In (a) and (b), the band structures of CoZrBi without and with SOC plotted along $\frac{2\pi}{a}(0.3, 0.0, 1.0) - \frac{2\pi}{a}(0.0, 0.0, 1.0) - \frac{2\pi}{a}(0.0, 0.3, 1.0)$ path, which is along the path $W \leftarrow X \rightarrow W$. In (e) and (f) the band structures of SiLiIn without and with SOC are plotted along $\frac{2\pi}{a}(0.075, 0.0, 1.0) - \frac{2\pi}{a}(0.0, 0.0, 1.0) - \frac{2\pi}{a}(0.0, 0.075, 1.0)$ direction. The band structure obtained from the DFT calculation are plotted with dots while the band structure obtained from the $\mathbf{k}\cdot\mathbf{p}$ model Hamiltonian are plotted with dashed lines. In (c) and (d), the inner and outer branches of ST of CoZrBi around the X point in the conduction band minimum (CBM) are shown. (g) and (h), displays the same spin-texture for SiLiIn.

to the principle axis ($C'_2(x), C'_2(y)$), reflection in the dihedral plane (M_{d1}, M_{d2}), four fold rotation followed by reflection through a plane perpendicular to the principle axis $S_4(z)$. All the symmetries are listed in Table II. The symmetry operations listed in Table II, keep the linear Dresselhaus Hamiltonian $H_D(k)$ invariant. Further Table II reveal that out of plane spin component is zero, as no linear combination of k_x and k_y with σ_z is invariant under the symmetry operations. The effective Hamiltonian is,

$$H_X(k) = H_0(k) + \alpha_D(\sigma_x k_x - \sigma_y k_y) \quad (1)$$

where H_0 is the Hamiltonian of the free electrons with the dispersion $E_0(k) = \frac{\hbar^2}{2m^*} \left(k_x^2 + k_y^2 + \left(\frac{2\pi}{a}\right)^2 \right)$ and α_D

is the Dresselhaus coupling constant. Diagonalisation of Eqn. 1 yield, $E(k)^\pm = E_0 \pm \alpha_D \sqrt{(k_x^2 + k_y^2)}$. The band structure obtained from the model Hamiltonian calculation around X point without and including SOC are shown with dashed lines in Figs. 4(a) and 4(b), respectively and it agrees well with the DFT calculations. The values of the Dresselhaus parameter (α_D) obtained from the model Hamiltonian is $\alpha_D = 0.26 \text{ eV}\text{\AA}$. The value of α_D calculated as twice the ratio between the shift in energy and momentum from DFT calculation, $\alpha_D = \frac{2\delta E}{\delta k} = 0.25 \text{ eV}\text{\AA}$, is in a good agreement with that obtained from the $\mathbf{k}\cdot\mathbf{p}$ calculations.

Similarly, for the 8 electron system SiLiIn, the band structure of the CBM around the X point, in the absence and presence of SOC is displayed in Fig. 4[(e), (f)] respectively. The band splitting seen in Fig. 4(f) suggests Rashba-Dresselhaus effect. A comparison of ST shown in Fig. 4[(c), (d)] with Fig. 4[(g), (h)] reveal that the ST for 18 and 8 electrons are identical. As expected from the nature of band splitting the Dresselhaus parameter α_D is small and estimated to be $0.08 \text{ eV}\text{\AA}$. This small splitting is attributed to the participation of the sp^3 hybridized states for SiLiIn in contrast to the d states for CoZrBi, where the strength of SOC is expected to be higher for the latter.

Using the model Hamiltonian Eqn. 1, we have calculated the band structure without and with SOC and

TABLE II. Symmetry operations of D_{2d} point group.

X point		
Symmetry operation	$\{k_x, k_y, k_z\}$	$\{\sigma_x, \sigma_y, \sigma_z\}$
$C_2(z) = -i\sigma_z$	$\{-k_x, -k_y, k_z\}$	$\{-\sigma_x, -\sigma_y, \sigma_z\}$
$C'_2(x) = -i\sigma_x$	$\{k_x, -k_y, k_z\}$	$\{\sigma_x, -\sigma_y, -\sigma_z\}$
$C'_2(y) = -i\sigma_y$	$\{-k_x, k_y, k_z\}$	$\{-\sigma_x, \sigma_y, -\sigma_z\}$
$S_4(z) = e^{i\frac{\pi}{4}\sigma_z}$	$\{k_y, -k_x, k_z\}$	$\{-\sigma_y, \sigma_x, \sigma_z\}$
$M_{d1} = -i \left(\frac{-\sigma_x + \sigma_y}{\sqrt{2}} \right)$	$\{k_y, k_x, k_z\}$	$\{-\sigma_y, -\sigma_x, -\sigma_z\}$
$M_{d2} = -i \left(\frac{\sigma_x + \sigma_y}{\sqrt{2}} \right)$	$\{-k_y, -k_x, k_z\}$	$\{\sigma_y, \sigma_x, -\sigma_z\}$

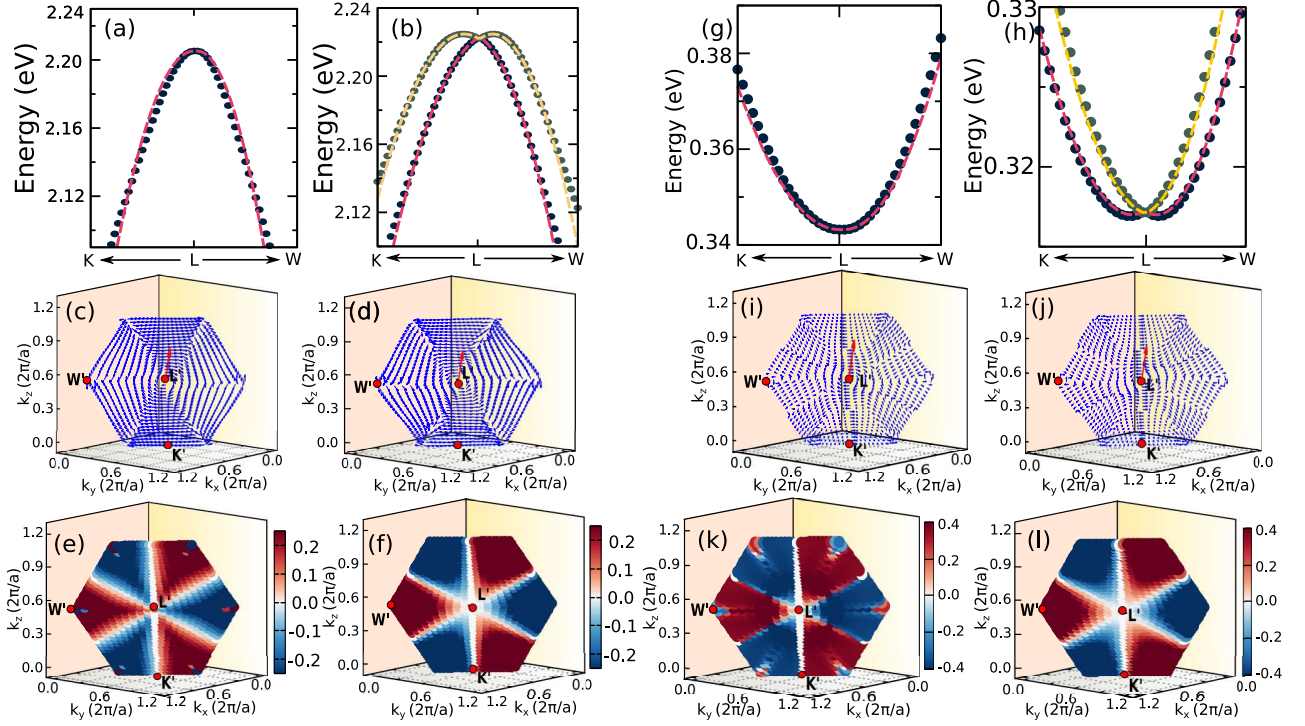


FIG. 5. ((a), (b)) Band structure without and with SOC for the conduction band for CoZrBi is plotted along $\frac{2\pi}{a}(0.563, 0.563, 0.374)$ - $(\frac{2\pi}{a}(0.5, 0.5, 0.5))$ - $\frac{2\pi}{a}(0.623, 0.377, 0.5)$ which lies along the path $K \leftarrow L \rightarrow W$. Band structure obtained from DFT is plotted with dots and the band structure obtained from the $\mathbf{k} \cdot \mathbf{p}$ model Hamiltonian is plotted with dashed lines. ((c), (d)) ST of inner and outer branches around L' point for CoZrBi for the conduction band obtain from DFT calculation. ((e), (f)) Out-of-plane spin component of CoZrBi in the plane defined by $k_x + k_y + k_z = \frac{3\pi}{a}$, obtained from DFT and model Hamiltonian respectively. ((g), (h)) Band structure without and with SOC for the conduction band for SiLiIn is plotted along $\frac{2\pi}{a}(0.531, 0.531, 0.437)$ - $(\frac{2\pi}{a}(0.5, 0.5, 0.5))$ - $\frac{2\pi}{a}(0.56, 0.44, 0.5)$ which lies along the path $K \leftarrow L \rightarrow W$. ((i), (j)) ST of inner and outer branches around L' point for SiLiIn in the conduction band. (k), (l) Out-of-plane spin component of SiLiIn in the plane defined by $k_x + k_y + k_z = \frac{3\pi}{a}$, obtained from DFT and model Hamiltonian respectively.

is shown with dotted line in Fig. 4[(e), (f)], which agrees well with the band structure obtained from the DFT calculations. Calculated Dresselhaus parameter from the model Hamiltonian, $\alpha_D = 0.08$ eVÅ, is in excellent agreement with the DFT estimate.

2. L point $(\frac{\pi}{a}, \frac{\pi}{a}, \frac{\pi}{a})$

Next we have focused around the polar L point of the conduction band of the 18 electron half-Heusler compound CoZrBi that features a local maximum. The DFT band structure without and with SOC is plotted in a narrow k -range around the neighbourhood of the high symmetry $L(\frac{\pi}{a}, \frac{\pi}{a}, \frac{\pi}{a})$ point along $W(\frac{2\pi}{a}, 0, \frac{\pi}{a})$ and $K(\frac{3\pi}{2a}, \frac{3\pi}{2a}, 0)$ directions as shown in Fig. 5(a) and 5(b) respectively. The nature of the SOC induced band splitting into two branches (see Fig. 5(b)) indicates the presence of either Rashba or Dresselhaus effect. We shall confirm the nature of the band splitting by calculating the spin textures in the framework of DFT supplemented with symmetry analysis within the $\mathbf{k} \cdot \mathbf{p}$ model. In order

to facilitate the plot of ST we have considered a plane \perp to the (111) direction, in such a way so that L point is at the origin of this plane given by $k_x + k_y + k_z = \frac{3\pi}{a}$. We define a co-ordinate system such that k'_x and k'_y are lying in the plane while k'_z is along (111) direction. The new coordinate system k'_x, k'_y , and k'_z is related to k_x, k_y , and k_z by a shift of origin and rotation preserving the local point group symmetry. The resulting unit vectors are $\widehat{k}'_x = \frac{\widehat{k}_x}{\sqrt{2}} - \frac{\widehat{k}_y}{\sqrt{2}}$, $\widehat{k}'_y = \frac{\widehat{k}_x}{\sqrt{6}} + \frac{\widehat{k}_y}{\sqrt{6}} - \frac{2\widehat{k}_z}{\sqrt{6}}$ and $\widehat{k}'_z = \frac{1}{\sqrt{3}}\widehat{k}_x + \frac{1}{\sqrt{3}}\widehat{k}_y + \frac{1}{\sqrt{3}}\widehat{k}_z$. As a consequence, the co-ordinate of the high symmetry points in this plane are $L'(0, 0, 0)$, $W'(\frac{\sqrt{2}\pi}{a}, 0, 0)$ and $K'(0, \frac{\sqrt{6}\pi}{2a}, 0)$. The corresponding spin textures are calculated for the two branches in the above mentioned plane around the L' point are shown in Fig. 5(c) and 5(d) respectively. The in-plane spin components exhibit distinct chiral configuration as expected for the Rashba ST, while the presence of the out-of-plane spin components with distinct pattern [Fig. 5(e) and (f)] suggests that higher order k terms may be involved. Moving from the inner to the outer branch direction, the chirality changes from clockwise to counter-

TABLE III. Symmetry operations of C_{3v} point group.

Symmetry operation	L point	
	$\{k'_x, k'_y, k'_z\}$	$\{\sigma'_x, \sigma'_y, \sigma'_z\}$
$C_3^+ ([111]) = e^{-i\frac{2\pi}{3}\sigma'_z}$	$\left\{ \left(-\frac{1}{2}k'_x + \frac{\sqrt{3}}{2}k'_y \right), \left(-\frac{\sqrt{3}}{2}k'_x - \frac{1}{2}k'_y \right), k'_z \right\}$	$\left\{ \left(-\frac{1}{2}\sigma'_x + \frac{\sqrt{3}}{2}\sigma'_y \right), \left(-\frac{\sqrt{3}}{2}\sigma'_x - \frac{1}{2}\sigma'_y \right), \sigma'_z \right\}$
$C_3^- ([111]) = e^{i\frac{2\pi}{3}\sigma'_z}$	$\left\{ \left(-\frac{1}{2}k'_x - \frac{\sqrt{3}}{2}k'_y \right), \left(\frac{\sqrt{3}}{2}k'_x - \frac{1}{2}k'_y \right), k'_z \right\}$	$\left\{ \left(-\frac{1}{2}\sigma'_x - \frac{\sqrt{3}}{2}\sigma'_y \right), \left(\frac{\sqrt{3}}{2}\sigma'_x - \frac{1}{2}\sigma'_y \right), \sigma'_z \right\}$
$\sigma = -i \left(-\frac{1}{2}\sigma'_x + \frac{\sqrt{3}}{2}\sigma'_y \right)$	$\left\{ \left(\frac{1}{2}k'_x + \frac{\sqrt{3}}{2}k'_y \right), \left(\frac{\sqrt{3}}{2}k'_x - \frac{1}{2}k'_y \right), k'_z \right\}$	$\left\{ \left(-\frac{1}{2}\sigma'_x - \frac{\sqrt{3}}{2}\sigma'_y \right), \left(-\frac{\sqrt{3}}{2}\sigma'_x + \frac{1}{2}\sigma'_y \right), -\sigma'_z \right\}$
$\sigma' = -i \left(-\frac{1}{2}\sigma'_x - \frac{\sqrt{3}}{2}\sigma'_y \right)$	$\left\{ \left(\frac{1}{2}k'_x - \frac{\sqrt{3}}{2}k'_y \right), \left(-\frac{\sqrt{3}}{2}k'_x - \frac{1}{2}k'_y \right), k'_z \right\}$	$\left\{ \left(-\frac{1}{2}\sigma'_x + \frac{\sqrt{3}}{2}\sigma'_y \right), \left(\frac{\sqrt{3}}{2}\sigma'_x + \frac{1}{2}\sigma'_y \right), -\sigma'_z \right\}$
$\sigma'' = -i\sigma'_x$	$\{-k'_x, k'_y, k'_z\}$	$\{\sigma'_x, -\sigma'_y, -\sigma'_z\}$

clockwise. In both the inner and outer branches, the spin is orthogonal to the wave vector \vec{k} , which is typical of Rashba-type SOC. The Rashba parameter estimated from the DFT calculation is found to be $\alpha_R=0.37$ eVÅ.

The $\mathbf{k}\cdot\mathbf{p}$ model Hamiltonian is constructed by preserving C_{3v} symmetry at the L point. The $\mathbf{k}\cdot\mathbf{p}$ Hamiltonian is defined in the reciprocal space (k'_x, k'_y, k'_z) as mentioned above, where the three-fold rotation (C_3) occurs around the trigonal axis k'_z (parallel to the $[111]$ direction) in both clockwise (C_3^+) and anticlockwise (C_3^-) directions. The point group symmetry also includes three mirror planes. One mirror plane lies in the $k'_y-k'_z$ plane and is defined as σ'' , while the other two mirror planes can be obtained by applying C_3 and C_3^2 operations to the initial mirror plane, and they are defined as σ and σ' , respectively. Under these symmetry operations, the momentum and spin operators undergo transformation as listed in Table III. Thus, the symmetry-adapted model Hamiltonian for the conduction band at the L point is,

$$\begin{aligned}
H_L^C(k) &= H_0(k) + H_{SOC}(k) \\
&= -\frac{\hbar^2}{2m^*} (k_x'^2 + k_y'^2) + \alpha_R (\sigma'_y k'_x - \sigma'_x k'_y) \\
&\quad + \gamma (k_x'^3 - 3k'_x k_y'^2) \sigma'_z
\end{aligned} \quad (2)$$

The cubic term in the effective Hamiltonian is included to explain the out-of-plane component σ'_z in the spin texture. The band structure without and with SOC obtained from the model Hamiltonian is shown with dotted line in Fig. 5(a) and Fig. 5(b) respectively, is in good agreement with the DFT band structure. The fitted Rashba parameter $\alpha_R=0.38$ eVÅ and $\gamma = -0.32$ eVÅ³ agrees well with the DFT estimate. Further the out of the plane component of ST obtained from DFT calculations is in reasonable agreement with that obtained from the model Hamiltonian (see Fig. 4(e) and 4(f)) suggesting the robustness of the low-energy $\mathbf{k}\cdot\mathbf{p}$ model Hamiltonian[Eqn. 2].

The band structure around the neighbourhood of the L point without and with SOC for the s-p half-Heusler SiLiIn is presented in Fig. 5(g) and (h) respectively. The band structure of the 8 electron compound has a minimum at the L-point in contrast to a local maximum for the 18 electron compound due to the involvement of sp^3 hybridized state and the calculated

Rashba parameter, $\alpha_R = 0.14$ eVÅ, which is much smaller compared to the 18 electron compound. The spin textures of the inner and outer branches around the L' point of the lowest conduction band is shown in Fig. 5 (i) and (j). In-plane spin components have a pronounced chiral spin configuration, whereas the presence of the out-of-plane spin component indicate the presence of higher-order k terms as discussed before for the 18 electron compound[see Fig. 5(k) and (l)].

Since the point group symmetry of SiLiIn is identical to 18 electron half-Heusler compound CoZrBi, we can easily obtain the model Hamiltonian for the 8 electron system around the L' point, where $H_0(k) = \frac{\hbar^2}{2m^*} (k_x'^2 + k_y'^2)$ and the H_{SOC} is identical to Eqn. 2. The band structure obtained from the model Hamiltonian agree well with the DFT band dispersion shown with dotted lines in Fig. 5((g), (h)). The fitted parameters are $\alpha_R = 0.15$ eVÅ and $\gamma = -0.51$ eVÅ³. The obtained Rashba parameter α_R agrees well with the DFT estimate.

While the model Hamiltonian captures the band dispersion for both the compounds accurately, however the out of plane component of the ST obtained from DFT calculation have additional features which is not reproduced by H_L^C suggesting the presence of symmetry allowed additional terms.

Next we have analysed the top most valence bands around the L point for CoZrBi and SiLiIn that displays a maximum. In the absence of SOC the 3-fold degenerate t_2 bands at the Γ point splits into a two fold degenerate and a singly degenerate band at the the L point; consistent with the C_{3v} symmetry of the L point(see Fig. 2(b) and 3(b)). Inclusion of SOC further splits the four fold degenerate $J = \frac{3}{2}$ bands at the Γ point into a pair of spin-orbit entangled doubly degenerate bands at the L-point (see Fig. 2(d) and 3(d)). From the Fig. 2(b) and 3(b) we find that the top of the valence band at the L point for CoZrBi is at the Fermi level, while for SiLiIn it lies about 1.7 eV below the VBM at the Γ point. So in the following we have discussed the SOC induced band structure and consequent spin texture only for the 18-electron compound CoZrBi.

In order to obtain further insights the DFT band dispersion of the top most valence bands are plotted in a narrow k-range around the neighborhood of the high symmetry $L(\frac{\pi}{a}, \frac{\pi}{a}, \frac{\pi}{a})$ point along $W(\frac{2\pi}{a}, 0, \frac{\pi}{a})$ and

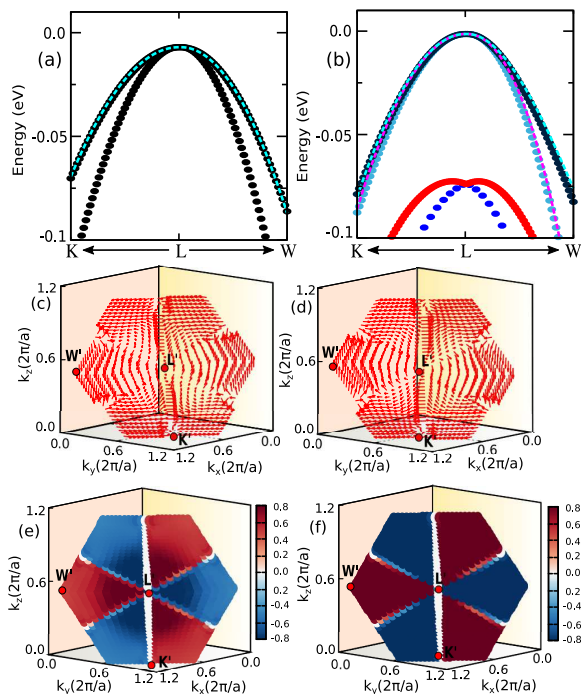


FIG. 6. ((a), (b)) Band structure without and with SOC for the valence band maxima for CoZrBi is plotted along $\frac{2\pi}{a}(0.538, 0.538, 0.425)$ - $(\frac{2\pi}{a}(0.5, 0.5, 0.5)$ - $\frac{2\pi}{a}(0.573, 0.427, 0.5)$ which lies along the path $K \leftarrow L \rightarrow W$. Band structure obtained from DFT is plotted with dots and the band structure obtained from the $\mathbf{k}\cdot\mathbf{p}$ model Hamiltonian is plotted with dashed lines. ((c), (d)) ST of inner and outer branches around L' point for CoZrBi obtained from DFT calculation. ((e), (f)) Out-of-plane spin component of CoZrBi in the plane defined by $k_x + k_y + k_z = \frac{3\pi}{a}$, obtained from DFT and model Hamiltonian respectively.

$K(\frac{3\pi}{2a}, \frac{3\pi}{2a}, 0)$ direction without and including SOC as shown in Fig. 6(a) and Fig. 6(b) respectively. Fig. 6(a) reveal a pair of doubly degenerate bands at the L point and the degeneracy is lifted upon inclusion of SOC (see Fig. 6(b)). It is interesting to note from Fig. 6(b) that the maxima of the topmost valence bands does not bifurcate away from the L point and remain at the L point, while for the lower two bands the maxima is bifurcated away from the L point displaying band crossing as expected for linear Rashba effect. This clearly establishes absence of linear Rashba effect for the topmost valence bands and therefore the leading term of the SOC Hamiltonian for the top most bands is expected to be cubic^{25,42}.

The plot of the DFT spintextures for the two bands around the L' point is illustrated in Fig. 6(c) and Fig. 6(d). Our calculations reveal that the in-plane spin-component exhibit characteristic chiral configuration with the presence of substantial out-of-plane spin component as illustrated in Fig. 6(e). In fact the out-of-plane component dominates over the in-plane component of $\langle \vec{S} \rangle$.

In order to corroborate our DFT results a $\mathbf{k}\cdot\mathbf{p}$ model Hamiltonian is constructed with cubic Rashba as the leading term respecting the C_{3v} symmetry at the L point²⁵. The symmetry adapted low energy $\mathbf{k}\cdot\mathbf{p}$ model Hamiltonian is :

$$H_L^v(k) = H_0(k) + \gamma(k_x'^3 - 3k_x'k_y'^2)\sigma_z' + \delta((k_x'^3 + k_x'k_y'^2)\sigma_y' - (k_y'^3 + k_y'k_x'^2)\sigma_x') \quad (3)$$

The band structure without and with SOC obtained from the model Hamiltonian for the topmost two bands are shown with dotted line in Fig. 6(a) and 6(b) respectively, and is in good agreement with DFT results. The calculated parameters of the model Hamiltonian are $\gamma=5.5 \text{ eV}\text{\AA}^3$ and $\delta=0.9 \text{ eV}\text{\AA}^3$ emphasizing the importance of the out-of-plane spin component. The out of plane component of the spin texture obtained from the model Hamiltonian shown in Fig. 6(f) is in reasonable agreement with the DFT spin texture shown in Fig. 6(e). The discovery of pure cubic Rashba splitting in non-polar half-Heusler alloys is rather unique and expected to find application in spintronics.

Similar results are obtained for the 8-electron compound SiLiIn where the splitting of the bands as expected is small.

B. Zeeman spin splitting

Till now we have discussed spin splitting and consequent spin textures around the time reversal invariant k-points, here we shall consider spin textures around the non time reversal invariant W point. The band structure of the top of the valence band of CoZrBi around the $W(\frac{\pi}{a}, \frac{2\pi}{a}, 0)$ point along the path $X(0, \frac{2\pi}{a}, 0)$ and $K(\frac{3\pi}{2a}, \frac{3\pi}{2a}, 0)$ all lying in the k_x - k_y plane without and including spin orbit coupling are displayed in Figs. 7(a) and 7(b) respectively. We find that the spin degeneracy of the bands are lifted upon inclusion of SOC. In contrast to the Rashba and Dresselhaus effect the spin splitting around the non-time reversal invariant W point does not have band crossing rather the splitting is identical to that realised in magnetic systems (i.e. in the absence of time reversal symmetry). Interestingly such a splitting is now realised in a non-magnetic system in the absence of inversion symmetry around a non-time reversal invariant high symmetry W point and will be designated as Zeeman splitting. It may be noted while the band structure around the W point in the k_x - k_y plane along the path X-W-K is identical to that plotted along $X(0, \frac{2\pi}{a}, 0)$ - $W(0, \frac{2\pi}{a}, \frac{\pi}{a})$ - $K(0, \frac{3\pi}{2a}, \frac{3\pi}{2a})$ lying in the k_y - k_z plane, the ST of the bands however are dominated by different spin components depending on the chosen plane. This is illustrated in Figs. 7[(c)-(e)] for the k_x - k_y plane and Fig. 7[(f)-(h)] for k_y - k_z plane where the primary contribution to the ST is from S_x and S_z components respectively.

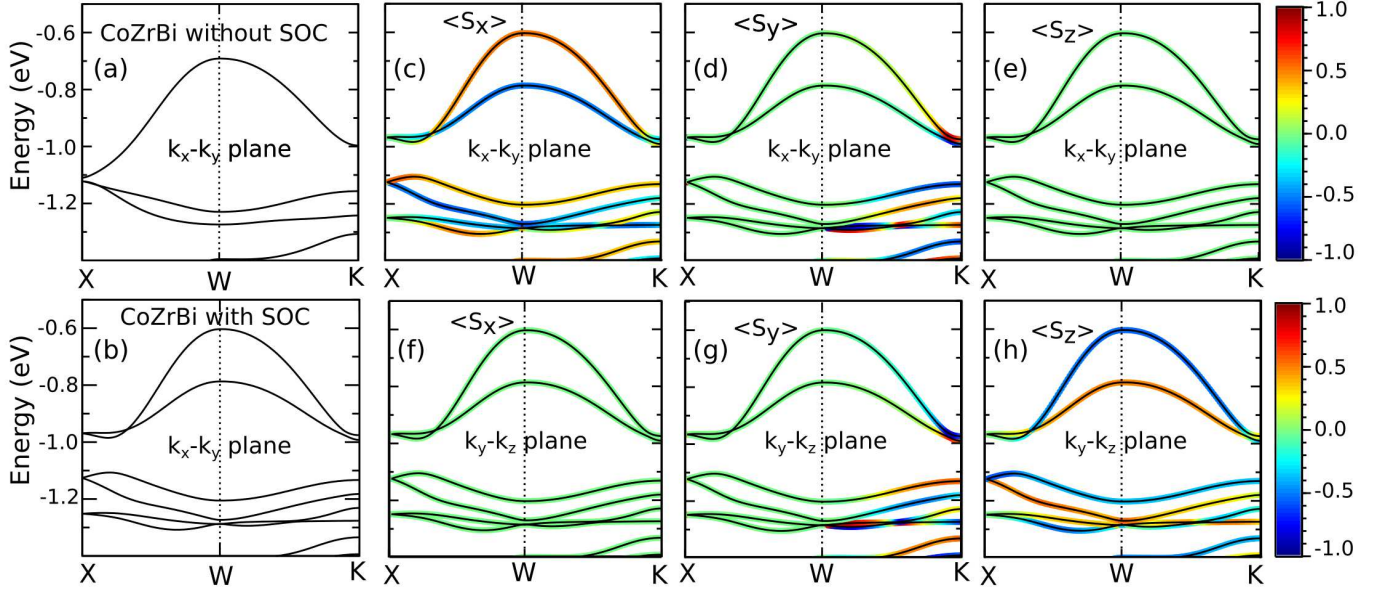


FIG. 7. (a), (b) Band structure without and with SOC in the valence band for CoZrBi is plotted along $\frac{2\pi}{a}(0.575, 0.575, 0.349)$ - $(\frac{2\pi}{a}(0.5, 0.5, 0.5)-\frac{2\pi}{a}(0.648, 0.351, 0.5))$ which lies along the path $K \leftarrow L \rightarrow W$. Band structure obtained from DFT is plotted with dashed lines and the band structure obtained from the $\mathbf{k}\cdot\mathbf{p}$ model Hamiltonian is plotted with dots. ((c), (d)) ST of inner and outer branches around L' point for CoZrBi for the conduction band obtained from DFT calculation. ((e), (f)) Out-of-plane spin component of CoZrBi in the plane defined by $k_x + k_y + k_z = \frac{3\pi}{a}$, obtained from DFT and model Hamiltonian respectively. ((g), (h)) Band structure without and with SOC for SiLiIn is plotted along $\frac{2\pi}{a}(0.563, 0.563, 0.374)-(\frac{2\pi}{a}(0.5, 0.5, 0.5)-\frac{2\pi}{a}(0.623, 0.377, 0.5))$ which lies along the path $K \leftarrow L \rightarrow W$. ((i), (j)) ST of inner and outer branches around L' point for SiLiIn in the conduction band. (k), (l) Out-of-plane spin component of SiLiIn in the plane defined by $k_x + k_y + k_z = \frac{3\pi}{a}$, obtained from DFT and model Hamiltonian respectively.

In order to explain the above observation we have calculated the effective SOC term allowed by symmetry around the W point. The point group symmetry around the W point is S_4 , which contains a two-fold rotation (C_2) around the principle axis. Additionally, there are two four-fold rotations (C_4) around the principal axis, one in the clockwise direction (C_4^+) and the other in the anticlockwise direction (C_4^-), followed by a reflection. The SOC term and the resulting SOC Hamiltonian²⁹ under the symmetry is,

$$\begin{aligned} \Omega_Z(\mathbf{k}) &= \lambda_Z [k_x(k_y^2 - k_z^2), k_y(k_z^2 - k_x^2) \\ &\quad , k_z(k_x^2 - k_y^2)] \\ H_W &= \mathbf{\Omega}_Z(\mathbf{k}) \cdot \boldsymbol{\sigma} \end{aligned} \quad (4)$$

where λ_Z is the Zeeman parameter. At the W point the splitting of the top two bands of CoZrBi is 186 meV as revealed from our DFT calculations. As the W point lies at the boundary of the BZ, therefore from the above Hamiltonian we can easily understand that effective magnetic field is more at the boundary, causing a large splitting. In order to understand the origin of SOC induced different spin textures in different planes we need to understand the symmetry associated with the chosen paths in the reciprocal space. The symmetry operations around the W point in the k_x - k_y plane along

$X(0, \frac{2\pi}{a}, 0)$ - $W(\frac{\pi}{a}, \frac{2\pi}{a}, 0)$ is C_{2x} . The spin components under the symmetry operation C_{2x} transforms like, $C_{2x} : (\sigma_x, \sigma_y, \sigma_z) \rightarrow (\sigma_x, -\sigma_y, -\sigma_z)$, ensuring primarily the σ_x component survives in the Hamiltonian. Using the model Hamiltonian in the k_x - k_y plane with $k_z = 0$, we focus on the $X(0, \frac{2\pi}{a}, 0) \rightarrow W(\frac{\pi}{a}, \frac{2\pi}{a}, 0)$ direction, where k_y is fixed and only k_x changes. This leads to an effective Hamiltonian around the W point and along the path XW, given by $H_W = \lambda_Z k_x k_y^2 \sigma_x$, assuming ($k_x \ll k_y = \frac{2\pi}{a}$). This suggest that the spin expectation value will be mostly contributed by the S_x component having positive value for the upper valence band around the W point, and negative for the lower valence band in agreement with DFT calculations shown in Figs. 7 [(c)-(e)]. Similarly for the the k_y - k_z plane, the Hamiltonian with ($k_z \ll k_y = \frac{2\pi}{a}$) will be given by $H_W = -\lambda_Z k_z k_y^2 \sigma_z$, as we move along the $X(0, \frac{2\pi}{a}, 0) \rightarrow W(0, \frac{2\pi}{a}, \frac{\pi}{a})$ direction where the valence band primarily has σ_z character. Here the expectation value of $\langle S_z \rangle$ is negative for the top of the valence band, while it is positive for the the lower valence band in agreement with our DFT results.

The results of our calculation for the 8 electron half-Heusler compound is shown in Fig. 8. A pair of valence bands around the W point exhibit Zeeman splitting upon application of SOC, where the splitting is more for the lower pair of bands. It is to be noted that splitting is weak in comparison to the 18 electron compound. Further the

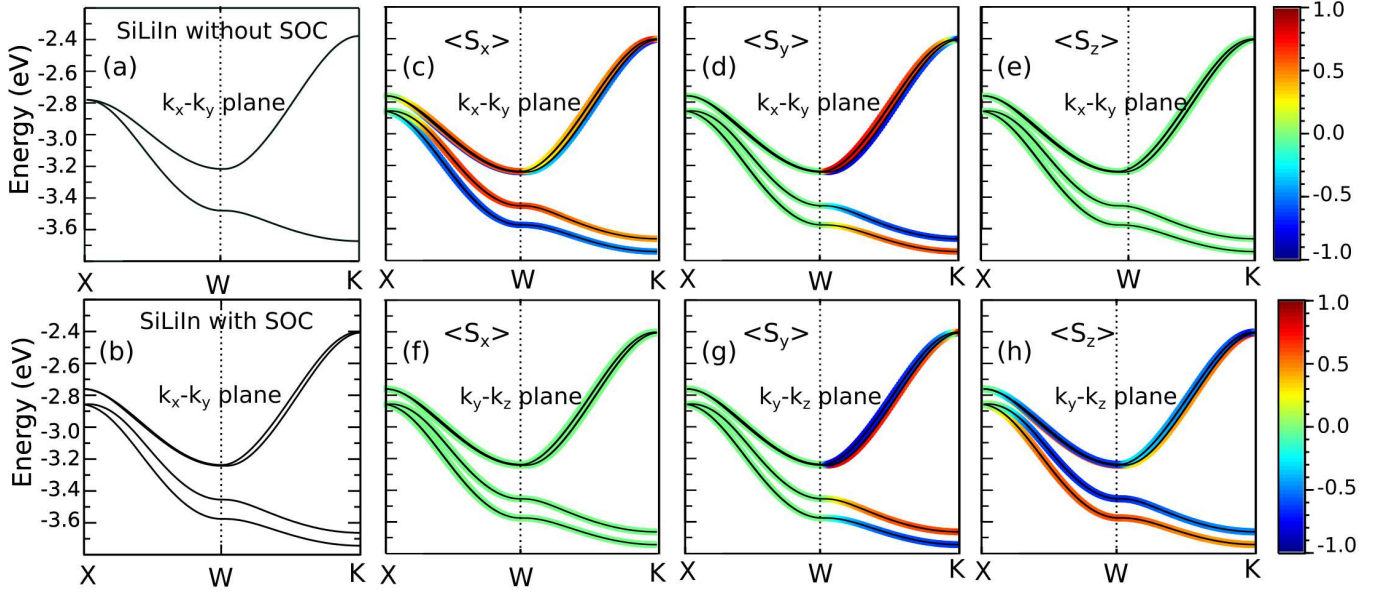


FIG. 8. Figure shows the band structure along with projected spin texture at non-time-reversal invariant k -point W of SiLiIn. Panels (a) and (b) show the band structure of SiLiIn with and without SOC along the path $X(0, \frac{2\pi}{a}, 0)$ - $W(\frac{2\pi}{a}, \frac{\pi}{a}, 0)$ - $K(\frac{3\pi}{2a}, \frac{3\pi}{2a}, 0)$. Panels ((c)-(e)) show the band structure with projected spin textures in the presence of SOC for SiLiIn along the path $X(0, \frac{2\pi}{a}, 0)$ - $W(\frac{\pi}{a}, \frac{2\pi}{a}, 0)$ - $K(\frac{3\pi}{2a}, \frac{3\pi}{2a}, 0)$ in the $k_x - k_y$ plane. Panels ((f)-(h)) show the band structure and spin textures in presence of SOC for SiLiIn along the path $X(0, \frac{2\pi}{a}, 0)$ - $W(0, \frac{2\pi}{a}, \frac{\pi}{a})$ - $K(0, \frac{3\pi}{2a}, \frac{3\pi}{2a})$ in the $k_y - k_z$ plane. The color code represents the orientation of the spin component.

nature of the spin textures are quite different from the 18 electron compound. In contrast to the 18 electron compound in the k_x - k_y plane, in addition to the $\langle S_x \rangle$ component there is appreciable $\langle S_y \rangle$ character [see Fig. 8(c-e)]. Similarly in the k_y - k_z plane in addition to the $\langle S_z \rangle$ character $\langle S_y \rangle$ character is also present[see Fig. 8(f-h)].

C. Band splitting with vanishing spin polarization(BSVSP)

The two half-Heusler systems considered here also exhibit another intriguing phenomenon namely band splitting with vanishing spin polarisation, where SOC splits the energy bands however both the split bands does not exhibit net spin polarisation along certain high symmetry directions of the BZ due to the presence of additional symmetries. In Fig. 9(a) the top of the valence band without SOC for CoZrBi along the path $A(\frac{\pi}{a}, \frac{\pi}{2a}, 0)$ - $\Gamma(0, 0, 0)$ - $L(\frac{\pi}{a}, \frac{\pi}{a}, \frac{\pi}{a})$ is displayed. In the absence of SOC the T_d symmetry at the Γ point splits the d bands into two fold degenerate e and three fold degenerate t_2 states. In Fig. 9(b) the same band structure including SOC is displayed. Inclusion of SOC further splits the t_2 states into two fold degenerate $J = \frac{1}{2}$ and four fold degenerate $J = \frac{3}{2}$ states, with the $J = \frac{1}{2}$ states lying lower in energy. Along the symmetry line Γ - L the $J = \frac{3}{2}$ states further split into three bands, where the lowest of the three is doubly degenerate. In Fig. 9(c)

we have shown the band structure projecting the $\langle S_x \rangle$ component of the spin. The expectation value of $\langle S_x \rangle$ vanishes for the top two spin split bands along Γ - L and the same is true for the other spin components. The vanishing expectation value of the spin $\langle \vec{S} \rangle$ for the two non-degenerate bands along Γ - L over each Bloch wave function leads to BSVSP.

In order to understand the origin of the vanishing spin polarisation we have constructed a $\mathbf{k}\cdot\mathbf{p}$ model Hamiltonian following Ref. 7,43. The $\mathbf{k}\cdot\mathbf{p}$ Hamiltonian for the $J = \frac{3}{2}$ manifold of the top of the valence band for the 18 electron compound CoZrBi in the vicinity of Γ point may be written as $H = H^+ + H^-$, where H^+ is invariant with respect to the spatial inversion,

$$H^+ = \frac{\hbar^2}{m} \left[\left(\gamma_1 + \frac{5}{2}\gamma_2 \right) \frac{1}{2}k^2 - \gamma_2 (k_x^2 J_x^2 + k_y^2 J_y^2 + k_z^2 J_z^2) \right. \\ \left. - 2\gamma_3 (\{k_x, k_y\} \{J_x, J_y\} + \{k_y, k_z\} \{J_y, J_z\} \right. \\ \left. + \{k_z, k_x\} \{J_z, J_x\}) \right] \quad (5)$$

and H^- breaks the spatial inversion symmetry,

$$H^- = -\frac{2C}{\sqrt{3}} [k_x \{J_x, V_x\} + k_y \{J_y, V_y\} \\ + k_z \{J_z, V_z\}] \quad (6)$$

Here, γ_1 , γ_2 , γ_3 and c are constants. J_x , J_y and J_z are 4×4 angular momentum matrices for a state of spin $\frac{3}{2}$, and k_x , k_y and k_z are the kinetic momentum terms. The symbol $\{a, b\}$ means the symmetrized

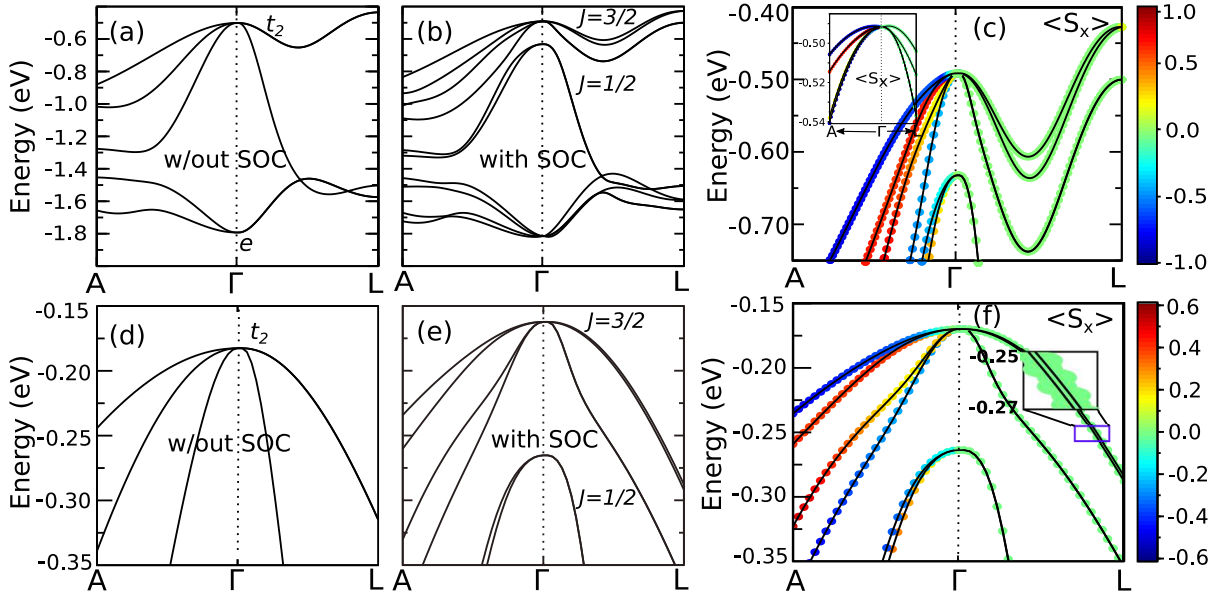


FIG. 9. Band splitting with vanishing spin polarization for 18- and 8 electron half-Heusler compounds. Panels (a) and (b) show the band structure of CoZrBi with and without SOC along the path $A(\frac{2\pi}{a}0.5, \frac{2\pi}{a}0.25, 0.0)-\Gamma(0, 0, 0)-L(\frac{2\pi}{a}0.5, \frac{2\pi}{a}0.5, \frac{2\pi}{a}0.5)$. Panels (d) and (e) show the band structure of SiLiIn with and without SOC along the path $A(\frac{2\pi}{a}0.5, \frac{2\pi}{a}0.25, 0.0)-\Gamma(0, 0, 0)-L(\frac{2\pi}{a}0.5, \frac{2\pi}{a}0.5, \frac{2\pi}{a}0.5)$. Panels (c) and (f) show the band structure and the x component of spin polarization for 18 electron and 8 electron compounds obtained from DFT, inset of this (c) represents the band structure and the x component of spin polarization obtain from $\mathbf{k}\cdot\mathbf{p}$ model Hamiltonian.

product $\frac{1}{2}(ab + ba)$. The quantities V_x, V_y and V_z are given by: $V_x = J_y^2 - J_z^2$, $V_y = J_z^2 - J_x^2$, $V_z = J_x^2 - J_y^2$. Here, we focus on the band degeneracy and spin polarization instead of the exact band dispersion. The DFT band structure in a narrow range around the Γ point along the path A- Γ -L can be reasonably reproduced with the fitted parameter values are $\gamma_1 = -9.0$, $\gamma_2 = 2.0$, $\gamma_3 = -1.9$, $\frac{\hbar^2}{m} = 1$ and $C = -0.05$ [see Fig.9(c) inset]. The qualitative results do not depend on the exact parameters. To investigate the microscopic origin of the vanishing spin polarization along the symmetry line Γ -L, we have calculated the on-site energy differences between the orbitals of two non-degenerate t_2 states with opposite spin orientations which can be regarded as the magnetic field acting locally on the chosen orbitals. From the calculations we find that the magnetic field on a given orbital vanishes. The local magnetic moments associated with these orbitals cancel with each other, resulting in a vanishing net spin polarization for the eigen state and vanishing local spin polarization for the magnetic Co atom. In agreement with the DFT results, the projection of the $\langle S_x \rangle$ component on the band structure obtained from the model Hamiltonian also vanishes supporting the validity of the low energy model Hamiltonian.

Similar results around the Γ point and along the path Γ -L is displayed by the 8 electron compound SiLiIn. In Fig. 9(d) the band structure without SOC is three-fold degenerate around the Γ point. Inclusion of SOC splits the three-fold degenerate t_2 bands into $J = \frac{3}{2}$ quartet

and $J = \frac{1}{2}$ doublet as shown in Fig. 9(e). The splitting induced by SOC is 0.10 eV. Along the path Γ -L, the top $J = \frac{3}{2}$ bands further splits into a pair of non-degenerate bands and a doubly degenerate band and the former exhibit BSVSP effect along Γ -L. The splitting is however much smaller in comparison to the 18 electron compound. (see inset of Fig. 9(f)).

Using the same model Hamiltonian as described for the 18 electron half-Heusler we can understand the origin of the BSVSP for SiLiIn. We find the SOC-induced effective magnetic field acting on two different p orbitals of the same atom are equal and opposite in strength along the Γ L path, resulting in a BSVSP⁷. The splitting of the bands depends on the strength of SOC, as a consequence BSVSP effect is much stronger (30 meV) for the 18-electron compound while it is 3 meV for the 8-electron compound SiLiIn and only 0.05 meV for GaAs, suggesting 18-electron compounds will be ideal candidate for experimental detection of BSVSP.

V. CONCLUSION

In the present paper we have analysed the electronic structure of two representative half-Heusler systems with 18 electrons and 8 electrons respectively in the presence of spin-orbit interaction. Our calculations reveal rich features in the electronic structure due to spin-momentum locking induced by SOC. Although both the compounds have identical crystal structure,

TABLE IV. Our result and available Rashba and Dresselhaus parameters in literature.

System	α_R (eVÅ) k - point	α_D (eVÅ) k - point	non-polar or polar	Reference
CoZrBi	0.38 $L(\frac{\pi}{a}, \frac{\pi}{a}, \frac{\pi}{a})$	0.26 $X(0, 0, \frac{2\pi}{a})$	non-polar	This work
SiLiIn	0.15 $L(\frac{\pi}{a}, \frac{\pi}{a}, \frac{\pi}{a})$	0.08 $X(0, 0, \frac{2\pi}{a})$	non-polar	This work
BiTeI	3.8 $\Gamma(0, 0, 0)$	0.00 $\Gamma(0, 0, 0)$	polar	18
GeTe	4.8 $Z(\frac{\pi}{a}, \frac{\pi}{a}, \frac{\pi}{a})$	0.00 $Z(\frac{\pi}{a}, \frac{\pi}{a}, \frac{\pi}{a})$	polar	21
HfO ₂	0.028 $T(0, \frac{\pi}{b}, \frac{\pi}{c})$	0.578 $T(0, \frac{\pi}{b}, \frac{\pi}{c})$	polar	24
LaWN ₃	0.31 $\Gamma(0, 0, 0)$	0.01 $\Gamma(0, 0, 0)$	polar	25
AlAs	0.00 $X(0, 0, \frac{2\pi}{a})$	0.01 $X(0, 0, \frac{2\pi}{a})$	non-polar	44
GaP	0.00 $X(0, 0, \frac{2\pi}{a})$	0.07 $X(0, 0, \frac{2\pi}{a})$	non-polar	44

the orbital composition of the valence and conduction bands are different for the 18 electron and the 8 electron system. This brings in subtle changes in the SOC induced band structures emphasizing the important role of orbitals. In addition, the BZ of the half-Heusler system admits diverse local symmetries (little group) leading to non-trivial splitting of the band structure due to SOC, resulting in novel spin textures around the valleys of the high symmetry k-points.

Around the X point we have observed Dresselhaus effect as expected for a non centrosymmetric and non-polar material⁴⁴ [see Table IV]. Using a symmetry adapted $\mathbf{k}\cdot\mathbf{p}$ model Hamiltonian around the high symmetry X point, we have calculated the band dispersion and the consequent ST. The model Hamiltonian only required linear terms to reproduce the DFT results, and the Dresselhaus parameter α_D for the 18 electron and the 8 electron system is calculated to be 0.26 eVÅ and 0.08 eVÅ respectively, in good agreement with DFT results.

Similar to the Dresselhaus effect, we have observed the Rashba effect in both half-Heusler systems around the polar $L(\frac{\pi}{a}, \frac{\pi}{a}, \frac{\pi}{a})$ point in the [111] plane. The Rashba effect features both linear and higher-order terms for the conduction band, but the strength of the higher-order term is found to be much weaker compared to the linear term. However for the topmost valence band at the L point we have identified cubic Rashba to be the leading term of the SOC Hamiltonian with novel spin texture. The identification of pure cubic Rashba splitting in

half-Heusler alloys is rather unique and are expected to play important role in spin transport. Further both the Dresselhaus and Rashba splitting is found to be much weaker for the 8 electron sp based compound in comparison to the 18 electron system.

At the non-TR invariant high symmetry point W, we observe Zeeman spin splitting. From the $\mathbf{k}\cdot\mathbf{p}$ model Hamiltonian, we have established that only the cubic terms are invariant under symmetry operations, and the component of spin orientation depends on the chosen plane.

Finally, we have observed the BSVSP along the high symmetry path Γ -L in both 18 electron and 8 electron half-Heusler systems. Around the Γ point the tetrahedral environment causes the d orbitals of the 18 electron half-Heusler to split into t_2 and e states while leaving the p states degenerate for the 8 electron half-Heusler compound. The SOC further splits the t_2 and p states into four fold degenerate $J = \frac{3}{2}$ and two fold degenerate $J = \frac{1}{2}$ states. Along the path Γ -L the four fold degenerate $J = \frac{3}{2}$ states further splits into two non degenerate and a two fold degenerate bands. The presence of a pair of non degenerate bands in the presence of SOC with the little group of the relevant k-point belonging to the non-pseudo polar point group leads to BSVSP⁷.

Our calculations reveal that the valence band and the conduction band of half-Heusler alloys at the various high symmetry points feature extrema (valleys) characterized by spin texture which are dependent on the location of the valleys in the k-space designated by a valley index. In the presence of SOC the spin splitting is tied to the valley index, requiring the scattering of charge carriers between valleys to have simultaneous spin flip and momentum transfer. This favors long valley life time required for valleytronics application. These valleys can be accessible by doping.

Our detailed first principle calculations complemented with $\mathbf{k}\cdot\mathbf{p}$ model Hamiltonian method for the two representative half-Heusler systems identifies in a family of ternary half-Heusler system with heavy elements another novel functionality for potential application in spin-valleytronics⁴⁵.

ACKNOWLEDGMENTS

K.D thanks Council of Scientific and Industrial Research (CSIR) for support through a fellowship (File No. 09/080(1178)/2020-EMR-I). I.D. thanks Science and Engineering Research Board (SERB) India (Project No. CRG/2021/003024) and Technical Research Center, Department of Science and Technology (TRC-DST) for support.

* current address: Theoretical Materials Physics, CESAM, University of Liège, Liège, Belgium

† sspid@iacs.res.in

- ¹ E. I. Rashba, *Sov. Phys.-Solid State* **2**, 1109 (1960).
- ² G. Dresselhaus, *Phys. Rev.* **100**, 580 (1955).
- ³ B. A. Bernevig, J. Orenstein, and S.-C. Zhang, *Phys. Rev. Lett.* **97**, 236601 (2006).
- ⁴ M. Hirayama, R. Okugawa, S. Ishibashi, S. Murakami, and T. Miyake, *Phys. Rev. Lett.* **114**, 206401 (2015).
- ⁵ P. ZEEMAN, *Nature* **55**, 347 (1897).
- ⁶ Y. Li, J. Ludwig, T. Low, A. Chernikov, X. Cui, G. Arefe, Y. D. Kim, A. M. van der Zande, A. Rigosi, H. M. Hill, S. H. Kim, J. Hone, Z. Li, D. Smirnov, and T. F. Heinz, *Phys. Rev. Lett.* **113**, 266804 (2014).
- ⁷ K. Liu, W. Luo, J. Ji, P. Barone, S. Picozzi, and H. Xiang, *Nature Communications* **10**, 5144 (2019).
- ⁸ G. Bihlmayer, O. Rader, and R. Winkler, *New Journal of Physics* **17**, 050202 (2015).
- ⁹ S. LaShell, B. A. McDougall, and E. Jensen, *Phys. Rev. Lett.* **77**, 3419 (1996).
- ¹⁰ Y. M. Koroteev, G. Bihlmayer, J. E. Gayone, E. V. Chulkov, S. Blügel, P. M. Echenique, and P. Hofmann, *Phys. Rev. Lett.* **93**, 046403 (2004).
- ¹¹ H. Nakamura, T. Koga, and T. Kimura, *Phys. Rev. Lett.* **108**, 206601 (2012).
- ¹² P. D. C. King, R. H. He, T. Eknapakul, P. Buaphet, S.-K. Mo, Y. Kaneko, S. Harashima, Y. Hikita, M. S. Bahrany, C. Bell, Z. Hussain, Y. Tokura, Z.-X. Shen, H. Y. Hwang, F. Baumberger, and W. Meevasana, *Phys. Rev. Lett.* **108**, 117602 (2012).
- ¹³ Y. C. Cheng, Z. Y. Zhu, M. Tahir, and U. Schwingenschlogl, *Europhysics Letters* **102**, 57001 (2013).
- ¹⁴ H. L. Zhuang, V. R. Cooper, H. Xu, P. Ganesh, R. G. Hennig, and P. R. C. Kent, *Phys. Rev. B* **92**, 115302 (2015).
- ¹⁵ Z. S. Popović, J. M. Kurdestany, and S. Satpathy, *Phys. Rev. B* **92**, 035135 (2015).
- ¹⁶ J. Nitta, T. Akazaki, H. Takayanagi, and T. Enoki, *Phys. Rev. Lett.* **78**, 1335 (1997).
- ¹⁷ A. D. Caviglia, M. Gabay, S. Gariglio, N. Reyren, C. Cancellieri, and J.-M. Triscone, *Phys. Rev. Lett.* **104**, 126803 (2010).
- ¹⁸ K. Ishizaka, M. S. Bahrany, H. Murakawa, M. Sakano, T. Shimojima, T. Sonobe, K. Koizumi, S. Shin, H. Miyahara, A. Kimura, K. Miyamoto, T. Okuda, H. Namatame, M. Taniguchi, R. Arita, N. Nagaosa, K. Kobayashi, Y. Murakami, R. Kumai, Y. Kaneko, Y. Onose, and Y. Tokura, *Nature Materials* **10**, 521 (2011).
- ¹⁹ M. Sakano, M. S. Bahrany, A. Katayama, T. Shimojima, H. Murakawa, Y. Kaneko, W. Malaeb, S. Shin, K. Ono, H. Kumigashira, R. Arita, N. Nagaosa, H. Y. Hwang, Y. Tokura, and K. Ishizaka, *Phys. Rev. Lett.* **110**, 107204 (2013).
- ²⁰ F.-X. Xiang, X.-L. Wang, M. Veldhorst, S.-X. Dou, and M. S. Fuhrer, *Phys. Rev. B* **92**, 035123 (2015).
- ²¹ D. Di Sante, P. Barone, R. Bertacco, and S. Picozzi, *Advanced Materials* **25**, 509 (2013).
- ²² M. Liebmann, C. Rinaldi, D. Di Sante, J. Kellner, C. Pauly, R. N. Wang, J. E. Boschker, A. Giussani, S. Bertoli, M. Cantoni, L. Baldrati, M. Asa, I. Vobornik, G. Panaccione, D. Marchenko, J. Sánchez-Barriga, O. Rader, R. Calarco, S. Picozzi, R. Bertacco, and M. Morgenstern, *Advanced Materials* **28**, 560 (2016).
- ²³ L. G. D. da Silveira, P. Barone, and S. Picozzi, *Phys. Rev. B* **93**, 245159 (2016).
- ²⁴ L. L. Tao, T. R. Paudel, A. A. Kovalev, and E. Y. Tsymbal, *Phys. Rev. B* **95**, 245141 (2017).
- ²⁵ S. Bandyopadhyay, A. Paul, and I. Dasgupta, *Phys. Rev. B* **101**, 014109 (2020).
- ²⁶ C. Mera Acosta, L. Yuan, G. M. Dalpian, and A. Zunger, *Phys. Rev. B* **104**, 104408 (2021).
- ²⁷ H. Yuan, M. S. Bahrany, K. Morimoto, S. Wu, K. Nomura, B.-J. Yang, H. Shimotani, R. Suzuki, M. Toh, C. Kloc, X. Xu, R. Arita, N. Nagaosa, and Y. Iwasa, *Nature Physics* **9**, 563 (2013).
- ²⁸ D. Xiao, G.-B. Liu, W. Feng, X. Xu, and W. Yao, *Phys. Rev. Lett.* **108**, 196802 (2012).
- ²⁹ C. Mera Acosta, A. Fazzio, and G. M. Dalpian, *npj Quantum Materials* **4**, 41 (2019).
- ³⁰ J.-W. Luo, G. Bester, and A. Zunger, *Phys. Rev. Lett.* **102**, 056405 (2009).
- ³¹ S. Bandyopadhyay and I. Dasgupta, *Phys. Rev. B* **103**, 014105 (2021).
- ³² M. Yazdani-Kachoei and S. Jalali-Asadabadi, *Journal of Alloys and Compounds* **828**, 154287 (2020).
- ³³ Vikram, B. Sahni, C. K. Barman, and A. Alam, *The Journal of Physical Chemistry C* **123**, 7074 (2019).
- ³⁴ G. Kresse and J. Hafner, *Phys. Rev. B* **47**, 558 (1993).
- ³⁵ G. Kresse and J. Furthmüller, *Phys. Rev. B* **54**, 11169 (1996).
- ³⁶ P. E. Blöchl, *Phys. Rev. B* **50**, 17953 (1994).
- ³⁷ G. Kresse and D. Joubert, *Phys. Rev. B* **59**, 1758 (1999).
- ³⁸ J. P. Perdew, K. Burke, and M. Ernzerhof, *Phys. Rev. Lett.* **77**, 3865 (1996).
- ³⁹ S. Vajna, E. Simon, A. Szilva, K. Palotas, B. Ujfalussy, and L. Szunyogh, *Phys. Rev. B* **85**, 075404 (2012).
- ⁴⁰ B. R. K. Nanda and I. Dasgupta, *Journal of Physics: Condensed Matter* **15**, 7307 (2003).
- ⁴¹ H. Zhu, R. He, J. Mao, Q. Zhu, C. Li, J. Sun, W. Ren, Y. Wang, Z. Liu, Z. Tang, A. Sotnikov, Z. Wang, D. Broido, D. J. Singh, G. Chen, K. Nielsch, and Z. Ren, *Nature Communications* **9**, 2497 (2018).
- ⁴² H. J. Zhao, H. Nakamura, R. Arras, C. Paillard, P. Chen, J. Gosteau, X. Li, Y. Yang, and L. Bellaiche, *Phys. Rev. Lett.* **125**, 216405 (2020).
- ⁴³ C. R. Pidgeon and S. H. Groves, *Phys. Rev.* **186**, 824 (1969).
- ⁴⁴ S. Mishra, S. Thulasi, and S. Satpathy, *Phys. Rev. B* **72**, 195347 (2005).
- ⁴⁵ F. Casper, T. Graf, S. Chadov, B. Balke, and C. Felser, *Semiconductor Science and Technology* **27**, 063001 (2012).